

# Popcorn EMRIs

## Transient Gravitational Wave Signals and Their Analysis in Schwartz Space

PAU AMARO SEOANE  <sup>1,2</sup> AND KOSTAS TZANAVARIS  <sup>3,4</sup>

<sup>1</sup> *Universitat Politècnica de València, Spain*

<sup>2</sup> *Max Planck Institute for Extraterrestrial Physics, Garching, Germany*

<sup>3</sup> *Albert-Einstein-Institut, Max-Planck-Institut für Gravitationsphysik, D-30167 Hannover, Germany*

<sup>4</sup> *Higgs Centre for Theoretical Physics, James Clerk Maxwell Building, Edinburgh EH9 3FD, UK*

### ABSTRACT

We investigate extreme-mass ratio inspirals (EMRIs) with orbital periods exceeding the observational timescale of mHz gravitational wave observatories. In their early, highly eccentric phases, these systems generate transient gravitational wave bursts during pericentre passages, separated by long quiescent intervals; we designate these signals “popcorn EMRIs.” We utilize a steady-state analytical model based on the continuity equation in phase space to estimate the population in a Milky Way-like galaxy. The normalization of this model is linked to the solution of the Fokker-Planck equation describing stellar relaxation. Adopting a conservative one-year observation baseline ( $P > 1$  year), we estimate the steady-state population of popcorn EMRIs. We forecast an observable burst rate of 5 to 44 events per year. The low duty cycle ( $\sim 10^{-4}$ ) confirms their manifestation as isolated transients. Individual bursts from the Galactic Centre exhibit high detectability. Analyzing these intrinsically transient signals demands a rigorous mathematical framework, as standard windowing techniques distort burst morphology. We establish an analytical foundation using standard smoothing techniques commonly used in real analysis. This yields the mathematically correct definition for the Fourier transform of transient signals, justifying the use of the direct Fourier transform without ad hoc windowing and ensuring the integrity of spectral analysis.

**Keywords:** Gravitational waves (692) — Gravitational wave sources (2392) — Galactic center (565) — Stellar dynamics (1596) — Black holes (162) — Fourier analysis (1964)

### 1. INTRODUCTION

The inspiral of a stellar-mass compact object into a massive black hole (MBH), known as an extreme-mass ratio inspiral (EMRI), represents a critical target for the Laser Interferometer Space Antenna (LISA). These systems provide unparalleled opportunities to probe the geometry of spacetime in the strong-field regime.

The evolution of EMRIs is dominated by the emission of gravitational waves (GWs). The timescale for this process scales strongly with the semi-major axis ( $T_{\text{GW}} \propto a^4$ ), implying that EMRIs spend the vast majority of their lifetime in the early stages of inspiral, characterized by wide orbits and long orbital periods  $P$ . Although the merger rate at the Galactic Centre (GC) is relatively low, the extended duration of the early inspiral phase suggests a substantial steady-state population

of Early EMRIs (E-EMRIs) may currently reside within the LISA frequency band (P. Amaro Seoane et al. 2024).

This work focuses on the subset of E-EMRIs whose orbital periods exceed the duration of observation,  $P > T_{\text{obs}}$ . We adopt a conservative baseline of  $T_{\text{obs}} = 1$  year for primary analysis, while also considering the nominal 4-year mission duration. EMRIs are generally formed with very high eccentricities. In such configurations, the GW emission is concentrated into brief, intense bursts during the pericentre passage, which has a duration  $dt_{\text{peri}}$ . When  $dt_{\text{peri}} \ll T_{\text{obs}} < P$ , the observable signal consists of isolated transient events separated by extended periods of quiescence. We designate these discontinuous sources as “popcorn EMRIs”.

We estimate the population and detection rate of popcorn EMRIs at the GC using steady-state distribution models derived from the continuity equation in phase space. These estimates rely on analytical models that necessarily simplify the complex dynamics of the Galac-

tic Centre; therefore, the derived numbers must be interpreted as illustrative rather than definitive. We subsequently analyze their observational signatures, calculating the expected burst rate, duty cycle, and signal-to-noise ratios.

The spectral analysis of these transient signals presents significant challenges. Conventional Fourier techniques are optimized for continuous signals. When analyzing finite segments of continuous data, standard practice involves the application of window functions (tapering) to mitigate spectral leakage. However, popcorn EMRIs are intrinsically transient. Applying windowing techniques to these bursts distorts the physical morphology of the signal and can lead to substantial underestimation of the signal energy and SNR.

To address this fundamental issue, we develop a mathematical apparatus using based on standard smoothing techniques, in the theory of tempered distributions. This formalism provides a mathematically sound definition for the Fourier transform of transient and potentially discontinuous bursts. It circumvents the artifacts associated with ad hoc windowing and justifies the application of the direct Fourier transform for the spectral analysis of these signals.

## 2. ASTROPHYSICAL ESTIMATION OF THE POPCORN EMRI POPULATION

We derive an estimate for the steady-state population of popcorn EMRIs in a Milky Way-like galaxy based on the analytical astrophysical model presented in [P. Amaro Seoane et al. \(2024\)](#). This calculation relies on necessary simplifications regarding the stellar distribution and mass function. We utilize an illustrative two-component model ( $10 M_{\odot}$  and  $40 M_{\odot}$ ). We perform the analysis for two observational timescales: a conservative  $T_{\text{obs}} = 1$  year and the nominal  $T_{\text{obs}} = 4$  years.

### 2.1. Model Parameters and Definitions

We consider a central MBH of mass  $M_{\text{BH}} = 4.3 \times 10^6 M_{\odot}$ . We adopt an influence radius  $R_h = 3$  pc, consistent with current observations of the Galactic Centre ([R. Genzel et al. 2010](#)). The population model adopted from [P. Amaro Seoane et al. \(2024\)](#) divides EMRIs into three regimes based on the semi-major axis  $a$ :  $N_I$  (circular,  $a < a_{\text{thr}}$ ),  $N_{II}$  (eccentric, detectable,  $a_{\text{thr}} < a < a_{\text{band}}$ ), and  $N_{III}$  (eccentric, early stage,  $a_{\text{band}} < a < a_{\text{crit}}$ ).

The steady-state distribution of EMRIs is derived from the continuity equation in the phase space of semi-major axis  $a$  ([P. Amaro Seoane et al. 2024](#)). In the eccentric regimes ( $N_{II}$  and  $N_{III}$ ), where the evolution is dominated by gravitational wave emission, this analysis yields  $dN/da \propto a^{-1/2}$ . This scaling arises because the

steady-state condition implies a constant flux of objects through energy space,  $\dot{a}(dN/da) = \text{constant}$ . For highly eccentric orbits near the loss cone, the time-averaged evolution rate scales as  $\dot{a} \propto a^{1/2}$  within the model's approximations ([P. Amaro Seoane 2019](#)). This analytical result is consistent with findings from numerical simulations ([F. Zhang & P. Amaro Seoane 2025](#)). Consequently, the number of sources  $N(a_1, a_2)$  between semi-major axes  $a_1$  and  $a_2$  is:

$$N(a_1, a_2) \propto \int_{a_1}^{a_2} a^{-1/2} da = 2(a_2^{1/2} - a_1^{1/2}). \quad (1)$$

The analysis relies on the population estimates derived in [P. Amaro Seoane et al. \(2024\)](#), which incorporate the effects of MBH spin ( $s$ ) and orbital inclination ( $\iota$ ) via the function  $\mathcal{W}(\iota, s)$  ([P. Amaro Seoane et al. 2013](#)). These effects shape the normalization and boundaries of the steady-state populations  $N_{I,II,III}(s, \iota)$ .

### 2.2. Orbital Period Thresholds

We define the threshold for popcorn EMRIs by  $P > T_{\text{obs}}$ . We calculate the corresponding semi-major axes  $a_T$  using Kepler's third law.

$$a_{T,1\text{yr}} \approx 7.884 \times 10^{-4} \text{ pc}, \quad (2)$$

$$a_{T,4\text{yr}} \approx 1.987 \times 10^{-3} \text{ pc}. \quad (3)$$

Sources with  $a > a_T$  are popcorn EMRIs ( $N_{\text{pop}}$ ), and sources with  $a < a_T$  are continuous ( $N_{\text{mono}}$ ).

### 2.3. Population Analysis for $10 M_{\odot}$ Compact Objects

We utilize boundaries from [P. Amaro Seoane et al. \(2024\)](#):  $a_{\text{thr}} = 2.17 \times 10^{-6}$  pc and  $a_{\text{band}} = 4.52 \times 10^{-3}$  pc. We observe  $a_{\text{thr}} < a_T < a_{\text{band}}$  for both timescales.

In region  $N_{III}$  ( $a > a_{\text{band}}$ ), all sources are popcorn EMRIs.

In region  $N_{II}$  ( $a_{\text{thr}} < a < a_{\text{band}}$ ), the population is split by  $a_T$ . The fraction of popcorn EMRIs  $F_{II,\text{pop}}$  is:

$$F_{II,\text{pop}}(T_{\text{obs}}) = \frac{a_{\text{band}}^{1/2} - a_T^{1/2}}{a_{\text{band}}^{1/2} - a_{\text{thr}}^{1/2}}. \quad (4)$$

$$F_{II,\text{pop}}(1\text{yr}) \approx 0.5954; F_{II,\text{pop}}(4\text{yr}) \approx 0.3445.$$

We utilize the conservative ranges for  $R_h = 3$  pc:  $N_{II} \in [0.05, 0.45]$  and  $N_{III} \in [1, 8]$ . We evaluate the extrema of  $N_{\text{Pop},10}(s, \iota) = N_{III}(s, \iota) + F_{II,\text{pop}}N_{II}(s, \iota)$ , accounting for the anti-correlation between  $N_{II}$  and  $N_{III}$ . For  $T_{\text{obs}} = 1$  year,

$$N_{\text{Pop},10}^{\text{max}} \approx 8 + 0.5954 \times 0.05 \approx 8.030,$$

$$N_{\text{Pop},10}^{\text{min}} \approx 1 + 0.5954 \times 0.45 \approx 1.268.$$

For  $T_{\text{obs}} = 4$  years the results are not very different,

$$\begin{aligned} N_{\text{Pop},10}^{\text{max}} &\approx 8 + 0.3445 \times 0.05 \approx 8.017, \\ N_{\text{Pop},10}^{\text{min}} &\approx 1 + 0.3445 \times 0.45 \approx 1.155. \end{aligned}$$

#### 2.4. Population Analysis for $40M_{\odot}$ Compact Objects

We utilize boundaries from [P. Amaro Seoane et al. \(2024\)](#):  $a_{\text{thr}} = 5.59 \times 10^{-6}$  pc and  $a_{\text{band}} = 2.45 \times 10^{-4}$  pc. We observe  $a_{\text{band}} < a_T$  for both timescales.

In region  $N_{II}$ , all sources are continuous. In region  $N_{III}$  ( $a > a_{\text{band}}$ ), the population is split by  $a_T$ . The continuous population is  $N_{III,\text{cont}} = N(a_{\text{band}}, a_T)$ . We use the steady-state ratio:

$$R_T(T_{\text{obs}}) = \frac{N_{III,\text{cont}}}{N_{II}} = \frac{a_T^{1/2} - a_{\text{band}}^{1/2}}{a_{\text{band}}^{1/2} - a_{\text{thr}}^{1/2}}. \quad (5)$$

$R_T(1\text{yr}) \approx 0.9351$ ;  $R_T(4\text{yr}) \approx 2.177$ . The total popcorn population is  $N_{\text{Pop},40}(s, t) = N_{III}(s, t) - R_T N_{II}(s, t)$ . We utilize the conservative ranges:  $N_{II} \in [5, 45]$  and  $N_{III} \in [250, 2000]$ . Hence, for  $T_{\text{obs}} = 1$  year:

$$\begin{aligned} N_{\text{Pop},40}^{\text{max}} &\approx 2000 - 0.9351 \times 5 \approx 1995.3, \\ N_{\text{Pop},40}^{\text{min}} &\approx 250 - 0.9351 \times 45 \approx 207.9. \end{aligned}$$

For  $T_{\text{obs}} = 4$  years the results are again similar,

$$\begin{aligned} N_{\text{Pop},40}^{\text{max}} &\approx 2000 - 2.177 \times 5 \approx 1989.1, \\ N_{\text{Pop},40}^{\text{min}} &\approx 250 - 2.177 \times 45 \approx 152.0. \end{aligned}$$

#### 2.5. Total Estimated Population and Limitations

We sum the contributions from the two illustrative masses,  $N_{\text{Pop},\text{Total}} = N_{\text{Pop},10} + N_{\text{Pop},40}$ , aligning the corresponding extrema. For  $T_{\text{obs}} = 1$  year:  $N_{\text{Pop},\text{Total}} \approx 209$  to 2003. For  $T_{\text{obs}} = 4$  years:  $N_{\text{Pop},\text{Total}} \approx 153$  to 1997.

We also calculate the total continuous population  $N_{\text{mono}}$  by summing the continuous components ( $N_I$ ,  $N_{II,\text{cont}}$ ,  $N_{III,\text{cont}}$ ) across both mass bins, utilizing the  $N_I$  ranges from the underlying model. For  $T_{\text{obs}} = 1$  year:  $N_{\text{mono}} \approx 10$  to 88. For  $T_{\text{obs}} = 4$  years:  $N_{\text{mono}} \approx 16$  to 144.

The population estimates derived here must be regarded as purely illustrative due to the inherent limitations of the underlying analytical steady-state model. The derivation relies on solving the continuity equation under several idealized assumptions. The normalization of the steady-state population  $N$  is proportional to the merger rate  $\Gamma$ , which depends strongly on the assumed

stellar density profile  $\rho(r) \propto r^{-\gamma}$  and the total number of compact objects  $N_0$ . Specifically, the analytical derivation of  $\Gamma$  (see [P. Amaro Seoane 2019](#)) shows a complex dependence on these poorly constrained parameters. Furthermore, the model assumes a sharp transition at the critical radius  $a_{\text{crit}}$  between relaxation-dominated and GW-dominated regimes. This transition is modeled by matching the fluxes,  $\mathcal{F}_{\text{GW}} = \mathcal{F}_{\text{relax}}$ , ignoring the interplay between these processes in the transition region. The model also employs a simplified two-component mass function,  $f(m) = c_1 \delta(m - 10M_{\odot}) + c_2 \delta(m - 40M_{\odot})$ . The scaling  $dN/da \propto a^{-1/2}$  is specific to the high-eccentricity limit ( $e \rightarrow 1$ ) and the adopted relaxation model. Deviations from these idealized conditions, such as anisotropies, are not captured, potentially leading to significant systematic uncertainties in the absolute number of sources.

### 3. OBSERVATIONAL SIGNATURES: POPCORN RATE AND DETECTABILITY

We analyze the observational characteristics of the E-EMRI population, utilizing the astrophysical estimates derived above and the scaling laws inherent to the steady-state, GW-dominated evolution.

#### 3.1. Population Model and Scaling Laws

The steady-state distribution in the eccentric, GW-dominated regime,  $dN/da \propto a^{-1/2}$ , implies a distribution of periods (using  $P \propto a^{3/2}$ ):

$$\frac{dN}{dP} = CP^{-2/3}. \quad (6)$$

Assuming  $P_{\text{min}} \ll T_{\text{obs}} \ll P_{\text{max}}$ , the continuous population is

$$N_{\text{mono}}(T_{\text{obs}}) = \int_{P_{\text{min}}}^{T_{\text{obs}}} CP^{-2/3} dP \approx 3CT_{\text{obs}}^{1/3}. \quad (7)$$

#### 3.2. Expected Rate

The expected number of popcorn bursts  $N_{\text{burst}}$  observed during  $T_{\text{obs}}$  from the population ( $P > T_{\text{obs}}$ ) is:

$$N_{\text{burst}}(T_{\text{obs}}) = \int_{T_{\text{obs}}}^{P_{\text{max}}} \frac{T_{\text{obs}}}{P} \frac{dN}{dP} dP \approx \frac{3}{2} CT_{\text{obs}}^{1/3}. \quad (8)$$

The ratio of expected bursts to continuous sources is independent of  $T_{\text{obs}}$  under these assumptions:

$$\frac{N_{\text{burst}}}{N_{\text{mono}}} \approx \frac{1}{2}. \quad (9)$$

The average burst rate is  $\mathcal{R} = N_{\text{burst}}/T_{\text{obs}} \propto T_{\text{obs}}^{-2/3}$ .

Using the derived ranges for  $N_{\text{mono}}$ , for  $T_{\text{obs}} = 1$  year ( $N_{\text{mono}} \in [10, 88]$ ),  $\mathcal{R} \approx 5$  to 44 per year. For  $T_{\text{obs}} = 4$  years ( $N_{\text{mono}} \in [16, 144]$ ):  $\mathcal{R} \approx 2$  to 18 per year.

### 3.3. Duty Cycle

We estimate the duty cycle  $D = \mathcal{R}\langle dt_{\text{peri}} \rangle$ . We estimate a typical duration for the population around Sgr A\* ( $M = 4.3 \times 10^6 M_{\odot}$ ).  $T_M = GM/c^3 \approx 21.18$  s. For a representative pericentre  $R_p = 10 GM/c^2$ , the burst duration is  $dt_{\text{peri}} \approx \sqrt{R_p^3/(2GM)}$ .

$$\langle dt_{\text{peri}} \rangle \approx T_M \sqrt{1000/2} \approx 474 \text{ s.} \quad (10)$$

The resulting duty cycles are for  $T_{\text{obs}} = 1$  year  $D \approx 7.5 \times 10^{-5}$ – $6.6 \times 10^{-4}$ . For  $T_{\text{obs}} = 4$  years:  $D \approx 3 \times 10^{-5}$ – $2.7 \times 10^{-4}$ . Since  $D \ll 1$  in all cases, the bursts are sparsely distributed and appear as isolated transient events.

### 3.4. Detectability

We estimate the detectability of individual bursts using an illustrative  $m = 10 M_{\odot}$  compact object at the Galactic Centre ( $D = 8.3$  kpc), orbiting the central MBH ( $M = 4.3 \times 10^6 M_{\odot}$ ). We assume a representative pericentre distance  $R_p = 10 GM/c^2$ . To fully characterize this system, we also define the orbital period  $P = 1$  year (the boundary case for  $T_{\text{obs}} = 1$  year), yielding an eccentricity  $e \approx 0.9974$ . The burst characteristics are determined using Keplerian approximations for the dynamics at closest approach.

The characteristic frequency of the burst,  $f_{\text{burst}}$ , corresponds to the inverse timescale of the pericentre passage. Kinematically, this is estimated as:

$$f_{\text{burst}} \approx \frac{1}{\pi} \sqrt{\frac{GM}{R_p^3}} = \frac{1}{10\sqrt{10\pi}} \frac{c^3}{GM}. \quad (11)$$

Using the gravitational timescale  $GM/c^3 \approx 21.18$  s, we find  $f_{\text{burst}} \approx 0.475$  mHz.

The effective duration of the gravitational wave emission during the passage is estimated by the fly-by timescale:

$$dt_{\text{peri}} \approx \sqrt{\frac{R_p^3}{2GM}} = \sqrt{500} \frac{GM}{c^3} \approx 474 \text{ s.} \quad (12)$$

The peak strain amplitude  $h$  is estimated using the leading-order quadrupole approximation for the emission at pericentre:

$$h \approx \frac{2G^2 M m}{c^4 D R_p} = \frac{1}{5} \frac{G m}{c^2 D} \approx 1.15 \times 10^{-17}. \quad (13)$$

The Signal-to-Noise Ratio (SNR) is formally defined by the matched filtering integral:

$$\text{SNR}^2 = 4 \int_0^\infty \frac{|\tilde{h}(f)|^2}{S_n(f)} df. \quad (14)$$

We employ two methods to estimate the SNR: a simple characteristic approximation and a detailed calculation based on the harmonic content.

First, we use the characteristic approximation for burst signals. This method estimates the total signal energy by assuming the noise spectral density  $S_n(f)$  is constant over the signal bandwidth, evaluated at  $f_{\text{burst}}$ . By Parseval's theorem, the energy integral in the frequency domain is related to the time integral  $\int |h(t)|^2 dt$ , which is approximated using the characteristic amplitude and duration,  $h^2 dt_{\text{peri}}$ . This yields:

$$\text{SNR}_{\text{char}}^2 \approx \mathcal{K} \frac{h^2 dt_{\text{peri}}}{S_n(f_{\text{burst}})}. \quad (15)$$

The factor  $\mathcal{K}$  accounts for polarization averaging, sky localization, and the precise relationship derived from the matched filter definition. We adopt  $\mathcal{K} = 1$  for this order-of-magnitude estimate.

The SNR depends critically on the LISA noise level at these low frequencies. We utilize the standard sky-averaged LISA sensitivity model, including instrumental noise (dominated by acceleration noise) and the Galactic confusion background. At  $f = 0.475$  mHz, we find  $S_n(f)^{1/2} \approx 1.1 \times 10^{-18} \text{ Hz}^{-1/2}$ . This is significantly higher than noise levels in the milli-Hertz bucket.

Using these values, the characteristic approximation yields:

$$\text{SNR}_{\text{char}} \approx 230. \quad (16)$$

Second, we calculate the SNR using the Peters formalism (P. C. Peters 1964) by summing the contributions from all harmonics of the orbital frequency. This method accurately accounts for the distribution of signal power across the spectrum and the frequency dependence of the detector noise  $S_n(f)$ .

$$\text{SNR}^2 \approx \frac{2G}{\pi^2 c^3 D^2} \sum_{n=1}^{\infty} \frac{\Delta E_n}{f_n^2 S_n(f_n)}. \quad (17)$$

The detailed calculation yields a significantly higher SNR:

$$\text{SNR} \approx 786. \quad (18)$$

The discrepancy between the two estimates (a factor of  $\approx 3.4$ ) highlights a limitation of the characteristic approximation when the noise curve is steep. The burst signal has a broad spectrum. Since the LISA noise increases sharply at lower frequencies, evaluating the noise solely at  $f_{\text{burst}}$  overestimates the effective noise. We find that 90% of the SNR is accumulated by  $f \approx 0.91$  mHz, where the noise level is nearly three times lower than at  $f_{\text{burst}}$ .

Individual popcorn events from this illustrative  $10 M_{\odot}$  population are potentially detectable with very high

SNR, although we caution that these estimates are based on idealized Keplerian dynamics and the quadrupole approximation for radiation. For comparison, a  $40 M_{\odot}$  object under the same conditions yields  $\text{SNR} \approx 3140$ .

#### 4. SPECTRAL ANALYSIS OF TRANSIENT SIGNALS

The analysis presented in this section addresses a critical requirement for the study of popcorn EMRIs: the definition of the Fourier transform for intrinsically transient signals. This foundational work is essential, not superfluous, because conventional spectral analysis techniques, optimized for continuous signals, fail to correctly capture the spectral content of isolated bursts. Applying standard practices like windowing introduces artifacts and distortions that compromise the physical interpretation of the signal.

We analyze the mathematical framework required for the frequency domain representation of popcorn EMRI signals. These emissions manifest as short bursts, potentially with discontinuities. Conventional spectral analysis techniques, developed primarily for continuous signals observed over finite times, must be applied with caution to intrinsically transient phenomena. We utilize the properties of the Schwartz functions to provide a basis for the Fourier transform of these bursts and contrast it with the issues of spectral leakage inherent in standard data analysis practices.

##### 4.1. Spectral Leakage and Windowing in Conventional Analysis

In gravitational wave data analysis, the Fourier transform (typically via the Fast Fourier Transform, FFT) is applied to finite segments of data (M. Maggiore 2008; E. Thrane & C. Talbot 2019). The analysis of an infinitely long, continuous signal  $h(t)$  over a finite duration  $T$  is mathematically equivalent to observing a windowed signal  $h_w(t)$ :

$$h_w(t) = h(t) \cdot \Pi_T(t), \quad (19)$$

where  $\Pi_T(t)$  is the rectangular window function (unity within the observation interval, zero otherwise).

By the convolution theorem, the observed spectrum  $\tilde{h}_w(f)$  is the convolution of the true spectrum  $\tilde{h}(f)$  and the Fourier transform of the window function:

$$\tilde{h}_w(f) = \tilde{h}(f) * \mathcal{F}\{\Pi_T(t)\}. \quad (20)$$

The Fourier transform of the rectangular window is the sinc function:

$$\mathcal{F}\{\Pi_T(t)\} = T \text{sinc}(\pi f T). \quad (21)$$

The sinc function possesses significant side lobes that decay only as  $1/f$ . The convolution in Eq. (20) smears

the true spectrum; power from a spectral feature at frequency  $f_0$  "leaks" into adjacent frequencies due to these side lobes. This phenomenon is spectral leakage.

In practice, the signal is also sampled at discrete times. This process is mathematically modeled by multiplying the continuous signal by a Dirac comb (Shah function),  $\text{III}_{\Delta t}(t) = \sum_{n=-\infty}^{\infty} \delta(t - n\Delta t)$ , where  $\Delta t$  is the sampling interval. The resulting analysis via the Discrete Fourier Transform (DFT) yields a spectrum characterized by the convolution with the Dirichlet kernel  $D_N(\omega)$ , which is the discrete-time Fourier transform of the rectangular window of length  $N$  samples:

$$D_N(\omega) = \frac{\sin(N\omega/2)}{\sin(\omega/2)}. \quad (22)$$

The Dirichlet kernel exhibits the same problematic side lobe behavior as the sinc function.

Spectral leakage is primarily driven by the sharp discontinuities introduced by the rectangular window at the boundaries of the observation interval when analyzing continuous signals. If the signal amplitude is non-zero at these boundaries, the windowing process creates artificial high-frequency content associated with the abrupt truncation.

Standard mitigation involves applying a taper function  $w(t)$  (e.g., Hann or Tukey) instead of the rectangular window. Tapers smoothly transition the signal to zero at the boundaries, reducing the discontinuities. The Fourier transforms of these taper functions have significantly suppressed side lobes compared to the Dirichlet kernel, thereby reducing long-range spectral leakage, albeit at the cost of broadening the main lobe (reducing frequency resolution).

##### 4.2. The Case of Popcorn EMRIs: Intrinsic Transients

The situation with popcorn EMRIs differs fundamentally. The signal  $h_{\text{burst}}(t)$  is intrinsically transient; it has significant amplitude only during the short pericentre passage  $dt_{\text{peri}}$  and is effectively zero otherwise. The morphology of the burst, including its start and end (even if modeled as discontinuous), represents physical characteristics of the signal, not artifacts of the data acquisition length.

Applying a taper function to an intrinsic burst signal fundamentally alters the data analysis problem. If a taper  $w(t)$  is applied to the segment containing the burst, the analyzed signal becomes:

$$h_{\text{tapered}}(t) = h_{\text{burst}}(t) \cdot w(t). \quad (23)$$

The resulting spectrum is  $\tilde{h}_{\text{tapered}}(f) = \tilde{h}_{\text{burst}}(f) * \tilde{w}(f)$ . This convolution with the taper's spectrum distorts the physical spectrum of the burst.

More critically, tapering inherently reduces the signal power. By Plancherel's theorem (or Parseval's identity), the total energy is preserved under the Fourier transform. Since  $|w(t)| \leq 1$  and the function is designed to approach zero at the boundaries, the total energy of the tapered signal is strictly less than the original signal (unless  $w(t) = 1$  everywhere, the rectangular window).

$$E_{\text{tapered}} = \int |h_{\text{tapered}}(t)|^2 dt < \int |h_{\text{burst}}(t)|^2 dt = E_{\text{burst}}. \quad (24)$$

This reduction in signal energy directly impacts detectability. The optimal Signal-to-Noise Ratio (SNR) is given by the matched filtering integral. If the analysis relies on the tapered spectrum or if templates are not matched to the tapered signal, the calculated SNR will be systematically underestimated:

$$\text{SNR}_{\text{tapered}}^2 < \text{SNR}_{\text{true}}^2. \quad (25)$$

This underestimation can be substantial. For example, a Hann window reduces the signal power by a factor of  $3/8$  (more than 60%), leading to a significant loss in detection efficiency and potential biases in parameter estimation.

For popcorn EMRIs, where the goal is to characterize the physical parameters encoded in the specific spectral shape of the burst, such distortion and energy loss are unacceptable. It is therefore essential to establish why the direct Fourier transform (equivalent to a rectangular window perfectly encompassing the burst) is the correct approach, rather than relying on ad hoc windowing practices borrowed from the analysis of continuous signals. We require a formalism that defines the Fourier transform of the intrinsic burst signal without artificial modification.

#### 4.3. The Schwartz Space Formalism

We analyze these signals using the density properties of Schwartz functions, which justifies the use of the direct Fourier transform (equivalent to using a rectangular window that fully encompasses the burst) for transient signals.

The *Schwartz space*  $\mathcal{S}(\mathbb{R})$  is the space of all smooth, *i.e.*, infinitely differentiable functions whose derivatives of any order vanish at infinity faster than every polynomial. More specifically a function  $f : \mathbb{R} \rightarrow \mathbb{C}$  is a *Schwartz function*, *i.e.*, an element of  $\mathcal{S}(\mathbb{R})$  if and only if

$$\sup_{t \in \mathbb{R}} |t^m f^{(n)}(t)| < +\infty, \quad (26)$$

for all non-negative integers  $m, n$ . A key property is that the Fourier transform operator  $\mathcal{F}$  maps continuously  $\mathcal{S}(\mathbb{R})$  onto itself.

Gravitational wave signals, particularly transients with compact support (which may be discontinuous), do not belong to  $\mathcal{S}(\mathbb{R})$ . However, they possess finite energy and duration, placing them within larger function spaces, specifically the spaces  $L^p(\mathbb{R})$  of  $p$ -integrable functions, consisting of all complex-valued functions  $f$  on  $\mathbb{R}$  satisfying  $\|f\|_{L^p} := [\int_{\mathbb{R}} |f|^p dt]^{1/p} < +\infty$ . For every such function  $f$ , its Fourier transform  $\mathcal{F}f$  can be defined by a density argument. The idea here is to construct a sequence  $(f_n)$  of smooth functions that converge to  $f \in L^p(\mathbb{R})$  in the norm  $\|\cdot\|_{L^p}$ , and then define  $\mathcal{F}f$  as the limit<sup>5</sup> of the sequence  $\mathcal{F}f_n$ . It is important here to note that, if  $1 \leq p \leq 2$ , then  $\mathcal{F}$  is a continuous operator mapping  $L^p(\mathbb{R})$  to  $L^q(\mathbb{R})$ , where  $q$  is the Hölder conjugate of  $p$  satisfying  $1/p + 1/q = 1$ . This is a consequence of the Hausdorff-Young inequality.<sup>6</sup>

To approximate a function  $f \in L^p(\mathbb{R})$ , we first pick a smooth function  $\lambda : \mathbb{R} \rightarrow \mathbb{R}$  satisfying  $\int_{\mathbb{R}} \lambda(t) dt = 1$  and define  $\phi_n(t) = \sqrt{n} \lambda(\sqrt{n}t)$ . The sequence  $\phi_n$  is commonly referred to as an approximate identity that formally converges to the delta function. Then one can show that the function:

$$f_n(t) := (f * \phi_n)(t) = \int_{-\infty}^{+\infty} f(t') \phi_n(t - t') dt' \quad (27)$$

is a smooth function in  $L^p(\mathbb{R})$  for every integer  $n > 0$ , thus forming a sequence  $(f_n)$  that converges to  $f$  in the  $L^p$  norm (see [E. Lieb & M. Loss \(2001\) Theorem 2.16](#)).

This construction provides the mechanism for defining the Fourier transform of the transient signal via the limit of the transforms of the smoothed approximations, establishing that the standard Fourier integral (the direct Fourier transform) is the appropriate tool for their spectral analysis. This demonstrates why the smoothing by Schwartz functions is required: it provides the basis for analyzing transient signals without the distortions introduced by ad-hoc windowing.

#### 5. ILLUSTRATION: ANALYSIS OF A RECTANGULAR PULSE

We consider a transient pulse represented by a rectangular function:

$$f(t) = A \cdot \chi_{[-T/2, T/2]}(t), \quad (28)$$

<sup>5</sup> Given that  $\mathcal{S}(\mathbb{R})$  is a dense subspace of the space  $\mathcal{S}'(\mathbb{R})$ , this limit always exists and is generally a tempered distribution, not necessarily a function. However, the Fourier transforms of functions we are concerned with will always be integrable functions.

<sup>6</sup> See [M. Reed & B. Simon \(1972\) Theorem IX.8](#).

where  $\chi_I(t)$  is the characteristic function of the interval  $I$ . This function is in  $L^p(\mathbb{R})$  but not in  $\mathcal{S}(\mathbb{R})$  since it's discontinuous at  $t = \pm T/2$ .

We select the sequence of normalized Gaussian functions as the approximate identity, which is an element of the Schwartz space:

$$\phi_n(t) = \sqrt{n/\pi} e^{-nt^2} \in \mathcal{S}(\mathbb{R}). \quad (29)$$

The smooth approximating sequence  $(f_n)$  is generated by convolution  $f_n(t) = (f * \phi_n)(t)$ . Explicitly:

$$f_n(t) = \frac{A}{2} [\operatorname{erf}(\sqrt{n}(t+T/2)) - \operatorname{erf}(\sqrt{n}(t-T/2))]. \quad (30)$$

We calculate  $\mathcal{F}f_n(\omega)$  using the convolution theorem. Since  $f \in L^1(\mathbb{R})$  and  $\phi_n \in L^1(\mathbb{R})$ ,

$$\mathcal{F}f_n(\omega) = \mathcal{F}f_{L^1}(\omega) \cdot \mathcal{F}\phi_n(\omega), \quad (31)$$

where  $\mathcal{F}f_{L^1}(\omega)$  denotes the standard Fourier integral of  $f(t)$ . The Fourier transform of the Gaussian  $\phi_n(t)$  is

$$\mathcal{F}\phi_n(\omega) = e^{-\omega^2/(4n)}. \quad (32)$$

The Fourier integral of the rectangular pulse  $f(t)$  is

$$\mathcal{F}f_{L^1}(\omega) = AT \operatorname{sinc}(\omega T/2). \quad (33)$$

Thus, the Fourier transform of the smooth approximation is

$$\mathcal{F}f_n(\omega) = e^{-\omega^2/(4n)} \cdot AT \operatorname{sinc}(\omega T/2). \quad (34)$$

Notice that in the limit as  $n \rightarrow \infty$ , the sequence  $(\mathcal{F}f_n)$  converges to  $\mathcal{F}f_{L^1}(\omega)$ . This demonstrates how the smoothing techniques presented here define the Fourier transform of  $f(t)$  as the standard integral:

$$\mathcal{F}f(\omega) = AT \operatorname{sinc}(\omega T/2). \quad (35)$$

## 6. ILLUSTRATION: ANALYSIS OF A TRUNCATED SINUSOID

We analyze a transient signal modeled by a truncated sinusoidal wave:

$$f(t) = A \sin(\omega_0 t) \cdot \chi_{[0, T]}(t). \quad (36)$$

This function is bounded and has compact support, and is therefore in  $L^p(\mathbb{R})$  for all  $p \geq 1$ . We construct the smooth approximating sequence  $f_n(t) = (f * \phi_n)(t)$  using the Gaussian kernel  $\phi_n \in \mathcal{S}(\mathbb{R})$ . The Fourier transform of  $f_n(t)$  is

$$\mathcal{F}f_n(\omega) = e^{-\omega^2/(4n)} \cdot \mathcal{F}f_{L^1}(\omega), \quad (37)$$

where  $\mathcal{F}f_{L^1}(\omega)$  is the standard Fourier integral:

$$\mathcal{F}f_{L^1}(\omega) = \frac{A}{2} \left( \frac{1 - e^{i(\omega_0 - \omega)T}}{\omega_0 - \omega} + \frac{1 - e^{-i(\omega_0 + \omega)T}}{\omega_0 + \omega} \right). \quad (38)$$

The limit  $\lim_{n \rightarrow \infty} \mathcal{F}f_n(\omega)$  converges to Eq. (38), validating the use of the standard Fourier integral for this transient signal.

## 7. NUMERICAL VALIDATION OF THE SCHWARTZ SPACE FORMALISM

We validate the Schwartz space formalism through numerical simulation of a transient gravitational wave burst. We demonstrate the convergence of the smoothed approximations in both time and frequency domains.

### 7.1. Simulated Signal Parameters

We simulate a short gravitational wave strain signal  $h(t)$ , modeled as a truncated sinusoid (as defined in Eq. 36). The parameters are: amplitude  $A = 1.0 \times 10^{-21}$ , characteristic frequency  $f_0 = 50$  Hz ( $\omega_0 = 100\pi$  rad/s), and duration  $T = 0.5$  s. The strain  $h(t)$  starts at  $t_{\text{start}} = 0.5$  s and ends at  $t_{\text{end}} = 1.0$  s.

### 7.2. Numerical Smoothing and Convergence

We construct the smooth approximation  $h_n(t) = (h * \phi_n)(t)$ . In the frequency domain, the smoothing acts as a low-pass filter (Eq. 37). We require  $4n \gg \omega_0^2 \approx 98696$ .

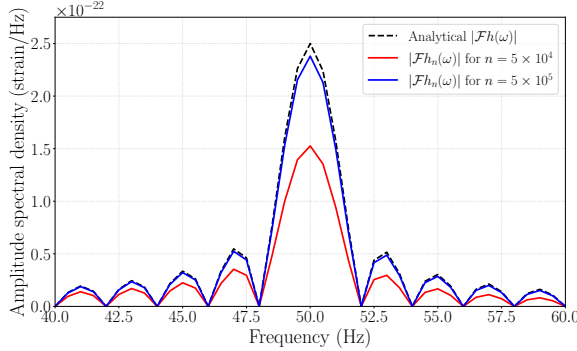
We select two values for the smoothing parameter:  $n_1 = 50000$  and  $n_2 = 500000$ . For  $n_1$ , the attenuation factor at  $\omega_0$  is  $e^{-\omega_0^2/(4n_1)} \approx 0.61$ . For  $n_2$ , the attenuation factor is  $e^{-\omega_0^2/(4n_2)} \approx 0.95$ .

Figure 1 shows the behavior of the smoothed signal  $h_n(t)$  compared to the original strain data  $h(t)$ . The convolution process regularizes the discontinuities. As  $n$  increases,  $h_n(t)$  converges closely to  $h(t)$ .

**Figure 1.** Time domain smoothing of the transient gravitational wave signal. The original discontinuous signal  $h(t)$  (black dashed line) is approximated by smooth functions  $h_n(t)$  for  $n = 5 \times 10^4$  (red solid line) and  $n = 5 \times 10^5$  (blue solid line). Convergence to  $h(t)$  improves as  $n$  increases.

### 7.3. Spectral Analysis

We compute the magnitude of the Fourier transform,  $|\mathcal{F}h(\omega)|$ . Figure 2 illustrates the convergence in the frequency domain. For  $n_1 = 50000$ , the spectrum shows attenuation near  $f_0 = 50$  Hz due to the Gaussian filter effect. For  $n_2 = 500000$ , the spectrum closely matches the analytical spectrum, confirming the convergence discussed in Section 4.



**Figure 2.** Frequency domain convergence of the Fourier transform magnitude. The analytical spectrum (black dashed line) is compared with the spectra of the smoothed signals for  $n = 5 \times 10^4$  (red solid line) and  $n = 5 \times 10^5$  (blue solid line). Attenuation caused by the smoothing decreases as  $n$  increases.

## 8. ANALYSIS OF EMRI BURSTS IN THE PETERS APPROXIMATION

We apply the technique of smoothing by Schwartz functions to analyze the gravitational wave signal corresponding to a single pericentre passage of a highly eccentric EMRI, modeled using the Peters quadrupole approximation.

### 8.1. Time-Domain Signal Definition and Transformation

We define the transient burst signal  $h(t)$  by isolating a single pericentre passage. The signal  $h(t)$  has compact support and finite energy, thus  $h(t) \in L^1(\mathbb{R}) \cap L^2(\mathbb{R})$ . The technique of smoothing by Schwartz functions established in Section 4 guarantees that the Fourier transform  $\mathcal{F}h(\omega)$  is defined and corresponds to the standard definition of the Fourier transform of integrable functions.

### 8.2. Harmonic Content in the Peters Approximation

We model the underlying orbital waveform using the quadrupole approximation. The power radiated in the  $n$ -th harmonic,  $L_n$ , is given by

$$L_n = \frac{32}{5} \frac{G^4 M^3 m^2}{c^5 a^5} g(n, e), \quad (39)$$

where  $g(n, e)$  is defined in terms of Bessel functions  $J_k(x)$ :

$$\begin{aligned} g(n, e) = \frac{n^4}{32} & \left\{ \left[ J_{n-2}(ne) - 2eJ_{n-1}(ne) + \frac{2}{n} J_n(ne) \right. \right. \\ & + 2eJ_{n+1}(ne) - J_{n+2}(ne) \left. \right]^2 \\ & + (1 - e^2) [J_{n-2}(ne) - 2J_n(ne) + J_{n+2}(ne)]^2 \\ & \left. \left. + \frac{4}{3n^2} J_n(ne)^2 \right] \right\}. \end{aligned} \quad (40)$$

### 8.3. Detectability

We estimate the detectability of individual bursts using an illustrative  $m = 10 M_\odot$  compact object at the Galactic Centre ( $D = 8.3$  kpc), orbiting the central MBH ( $M = 4.3 \times 10^6 M_\odot$ ). We assume a representative pericentre distance  $R_p = 10 GM/c^2$ . To fully characterize this system, we also define the orbital period  $P = 1$  year (the boundary case for  $T_{\text{obs}} = 1$  year), yielding an eccentricity  $e \approx 0.9974$ . The burst characteristics are determined using Keplerian approximations for the dynamics at closest approach.

The characteristic frequency of the burst,  $f_{\text{burst}}$ , corresponds to the inverse timescale of the pericentre passage. Kinematically, this is estimated as:

$$f_{\text{burst}} \approx \frac{1}{\pi} \sqrt{\frac{GM}{R_p^3}} = \frac{1}{10\sqrt{10}\pi} \frac{c^3}{GM}. \quad (41)$$

Using the gravitational timescale  $GM/c^3 \approx 21.18$  s, we find  $f_{\text{burst}} \approx 0.475$  mHz.

The effective duration of the gravitational wave emission during the passage is estimated by the fly-by timescale:

$$dt_{\text{peri}} \approx \sqrt{\frac{R_p^3}{2GM}} = \sqrt{500} \frac{GM}{c^3} \approx 474 \text{ s}. \quad (42)$$

The peak strain amplitude  $h$  is estimated using the leading-order quadrupole approximation for the emission at pericentre:

$$h \approx \frac{2G^2 M m}{c^4 D R_p} = \frac{1}{5} \frac{G m}{c^2 D} \approx 1.15 \times 10^{-17}. \quad (43)$$

The Signal-to-Noise Ratio (SNR) is formally defined by the matched filtering integral:

$$\text{SNR}^2 = 4 \int_0^\infty \frac{|\tilde{h}(f)|^2}{S_n(f)} df. \quad (44)$$

We employ two methods to estimate the SNR: a simple characteristic approximation and a detailed calculation based on the harmonic content.

First, we use the characteristic approximation for burst signals. This method estimates the total signal energy by assuming the noise spectral density  $S_n(f)$  is constant over the signal bandwidth, evaluated at  $f_{\text{burst}}$ . By Parseval's theorem, the energy integral in the frequency domain is related to the time integral  $\int |h(t)|^2 dt$ , which is approximated using the characteristic amplitude and duration,  $h^2 dt_{\text{peri}}$ . This yields:

$$\text{SNR}_{\text{char}}^2 \approx \mathcal{K} \frac{h^2 dt_{\text{peri}}}{S_n(f_{\text{burst}})}. \quad (45)$$

The factor  $\mathcal{K}$  accounts for polarization averaging, sky localization, and the precise relationship derived from the matched filter definition. We adopt  $\mathcal{K} = 1$  for this order-of-magnitude estimate.

The SNR depends critically on the LISA noise level at these low frequencies. We utilize the standard sky-averaged LISA sensitivity model, including instrumental noise (dominated by acceleration noise) and the Galactic confusion background. At  $f = 0.475$  mHz, we find  $S_n(f)^{1/2} \approx 1.39 \times 10^{-18}$  Hz $^{-1/2}$ . This is significantly higher than noise levels in the milli-Hertz bucket.

Using these values, the characteristic approximation yields:

$$\text{SNR}_{\text{char}} \approx 181. \quad (46)$$

Second, we calculate the SNR using the Peters formalism (P. C. Peters 1964) by summing the contributions from all harmonics of the orbital frequency. This method accurately accounts for the distribution of signal power across the spectrum and the frequency dependence of the detector noise  $S_n(f)$ .

$$\text{SNR}^2 \approx \frac{2G}{\pi^2 c^3 D^2} \sum_{n=1}^{\infty} \frac{\Delta E_n}{f_n^2 S_n(f_n)}. \quad (47)$$

The detailed calculation yields a significantly higher SNR:

$$\text{SNR} \approx 606. \quad (48)$$

The discrepancy between the two estimates (a factor of  $\approx 3.35$ ) highlights a limitation of the characteristic approximation when the noise curve is steep. The burst signal has a broad spectrum. Since the LISA noise increases sharply at lower frequencies, evaluating the noise solely at  $f_{\text{burst}}$  overestimates the effective noise. As shown in Figure 3, we find that 90% of the SNR is accumulated by  $f \approx 0.87$  mHz, where the noise level is approximately 2.5 times lower than at  $f_{\text{burst}}$ .

Individual popcorn events from this illustrative  $10 M_{\odot}$  population are potentially detectable with very high SNR, although we caution that these estimates are based on idealized Keplerian dynamics and the quadrupole approximation for radiation. For comparison, a  $40 M_{\odot}$  object under the same conditions yields  $\text{SNR} \approx 2423$ .

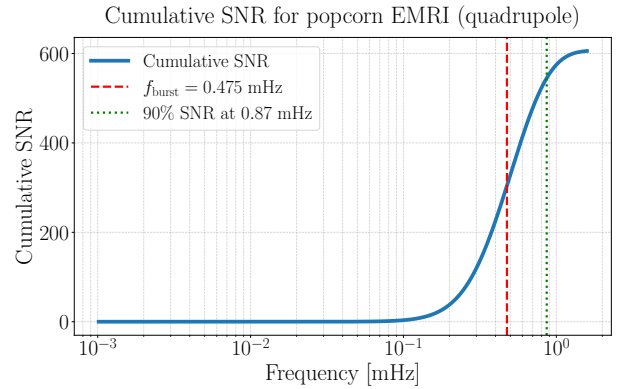


**Figure 3.** Cumulative SNR accumulation as a function of frequency for the illustrative popcorn EMRI system ( $10 M_{\odot}$ ,  $P = 1$  yr,  $e \approx 0.9974$ ) calculated using the Peters formalism. The characteristic frequency  $f_{\text{burst}}$  (red dashed line) is located where the noise curve is steep. 90% of the total SNR is accumulated by  $f \approx 0.87$  mHz (green dotted line), where the noise level is significantly lower.

## 9. CONCLUSIONS

This study presents an analysis of the population, detectability, and description of popcorn EMRIs—transient gravitational wave signals generated by long-period, highly eccentric inspirals. We have estimated the population of EMRIs with orbital periods exceeding the observational timescale, based on an analytical steady-state model of the Galactic Centre.

Based on a conservative, illustrative two-component model and a 1-year observation baseline, the predicted steady-state population of popcorn EMRIs ranges from approximately 209 to 2003. This significantly exceeds the estimated continuous EMRI population (10 to 88). The analysis indicates a steady-state distribution  $dN/dP \propto P^{-2/3}$ , implying that the expected number of detected bursts is approximately half the number of continuous sources. We forecast an observable burst rate of 5 to 44 events per year (for  $T_{\text{obs}} = 1$  year), decreasing to 2 to 18 per year (for  $T_{\text{obs}} = 4$  years). The low duty cycle ( $\sim 10^{-4}$ ) confirms their manifestation as isolated transients.

The proximity of the Galactic Centre suggests high detectability for individual bursts. We calculate the SNR using a realistic LISA noise model (including confusion noise). Using the Peters formalism we obtain substantial SNRs (SNR  $\approx 600$  for an illustrative system of  $10 M_{\odot}$ ).

We established the mathematical foundation for the frequency domain analysis of these transient signals using the theory of tempered distributions, and specifically the properties of Schwartz functions. This analysis is essential because standard data analysis practices, such as

windowing, are designed for finite segments of continuous data and are inappropriate for intrinsically transient signals. The point of this rigorous approach is to ensure that the analysis correctly captures the signal properties without distortion. We have demonstrated mathematically that windowing distorts the physical morphology of the burst and leads to significant underestimation of the SNR.

The smoothing techniques implemented here confirm that the direct Fourier transform is the spectral rep-

resentation of a transient event. This provides a solid foundation for data analysis strategies, dictating that tapering functions must be avoided when analyzing isolated popcorn EMRI bursts to prevent distortion of the waveform and biases in parameter estimation. This study establishes popcorn EMRIs as a potentially significant and detectable population of gravitational wave sources.

## REFERENCES

Amaro-Seoane, P. 2019, Phys.Rev.D., 99, 123025, doi: [10.1103/PhysRevD.99.123025](https://doi.org/10.1103/PhysRevD.99.123025)

Amaro Seoane, P., Lin, Y., & Tzanavaris, K. 2024, Physical Review D, 110, 064011

Amaro-Seoane, P., Sopuerta, C. F., & Freitag, M. D. 2013, Monthly Notices of the Royal Astronomical Society, 429, 3155

Genzel, R., Eisenhauer, F., & Gillessen, S. 2010, Reviews of Modern Physics, 82, 3121, doi: [10.1103/RevModPhys.82.3121](https://doi.org/10.1103/RevModPhys.82.3121)

Lieb, E., & Loss, M. 2001, Graduate Studies in Mathematics, Vol. 14, Analysis, 2nd edn. (American Mathematical Society)

Maggiore, M. 2008, Gravitational Waves: Volume 1: Theory and Experiments, Gravitational Waves (OUP Oxford). <https://books.google.de/books?id=AqVpQgAACAAJ>

Peters, P. C. 1964, Physical Review, 136, 1224

Reed, M., & Simon, B. 1972, Methods of Modern Mathematical Physics, Vol. I, Functional Analysis (Elsevier)

Thrane, E., & Talbot, C. 2019, PASA, 36, e010, doi: [10.1017/pasa.2019.2](https://doi.org/10.1017/pasa.2019.2)

Zhang, F., & Amaro Seoane, P. 2025, arXiv e-prints, arXiv:2510.10821, doi: [10.48550/arXiv.2510.10821](https://doi.org/10.48550/arXiv.2510.10821)